Chapter 3

Bolus- and frequency-based perfusion

This chapter had been adapted from:

Stowe, S., Boyle, A., Sage, M., See, W., Praud, J.-P., Fortin-Pellerin, É., & Adler, A. (2019). Comparison of bolus- and filtering-based EIT measures of lung perfusion in an animal model [Publisher: IOP Publishing]. Physiol. Meas., 40*(5), 054002*

3.1 Introduction

Electrical Impedance Tomography (EIT) uses electrical stimulation and measurements at electrodes on the body surface to reconstruct images of internal conductivity distribution and its changes. The most common application of EIT, experimentally and clinically, has been for imaging of the thorax (Frerichs *et al.*, 2017). Using a ring of electrodes around the chest, EIT is able to calculate images of impedance changes

in the abdomen. Although most research has focused on imaging of ventilation, there is significant interest in imaging cardiovascular phenomena with EIT (Adler *et al.*, 2012; Leonhardt and Lachmann, 2012).

EIT has been evaluated for its ability to measure cardiac output and lung perfusion since the early 90s (Eyüboğlu *et al.*, 1989; Frerichs *et al.*, 2002; Zadehkoochak *et al.*, 1992). Since then, various configurations of EIT have been evaluated (Borges *et al.*, 2012; Nguyen *et al.*, 2015). The effect of posture on EIT images was evaluated by Reifferscheid *et al.* (2011), who showed that changing posture introduces a large and reproducible variability into ventilation distribution as imaged by EIT. Based on results showing a common relationship between the effect of gravity and perfusion in both children and adults (Bhuyan *et al.*, 1989), in newborns we expect to see a comparable directional change in perfusion due to the changes in posture. Recently, Braun *et al.* (2018) evaluated EIT's ability to monitor cardiac output, showing that EIT is more reliable for monitoring cardiac output trends than absolute cardiac output. EIT has also been investigated for monitoring of systemic blood pressure (Solà *et al.*, 2011), and for monitoring of pulmonary arterial pressure (Proença *et al.*, 2017).

EIT measurements are sensitive to blood movement in two main ways. First, it is possible to image the transit of the contrast agent through the heart and lungs via a conductivity-contrasting bolus into the veins and second, through digital filtering of the time series of EIT images at the heart frequency (Leathard *et al.*, 1994). While multiple EIT measures of perfusion are used, their relationship is not well understood. It is currently unclear to what degree pulsatile impedance changes represent blood flow, and how they limit the potential for heart-frequency filtering

to correctly estimate the true perfusion (Nguyen *et al.*, 2012).

Injection of a contrast agent to measure regional lung perfusion has been compared with electron beam computed tomography (EBCT) and determined to be feasible for measuring perfusion across different animals (Frerichs *et al.*, 2002). Perfusion measurement via conductivity contrasts has the advantage of measuring the true perfusion, but requires placement of a catheter to introduce the contrast agent. Bolus-derived measurements cannot be made continuously because they rely upon the circulation of a contrast agent. In addition, the accumulation of NaCl (the main conductivity contrast used) over multiple injections can lead to hypernatremia which limits the rate at which bolus injections can be made.

Calculating the heart-frequency conductivity changes in the thorax offers the benefit of a continuous functional measure calculated directly from EIT signals (possibly in conjunction with a synchronization signal such as the ECG). Heart-frequency EIT signals are typically an order of magnitude smaller than ventilation signals; thus, when measurements are made during tidal ventilation, a large period of data must be used in order to reduce the ventilation signal. On the other hand, measurements during apnoea can be used to eliminate the ventilation signal, but for the safety of the patient the apnoea was limited to 30 s. In healthy human subject of less than one year old it takes a mean of 118 s for the blood oxygen saturation levels to drop below 90% (Fu *et al.*, 1996), however the length of safe apnoea is much shorter for the sick preterm infant. The time period was chosen based on experience in the lab showing that 30 s seconds was not associated with bradycardia or desaturation to less than 90% blood oxygen saturation.

There is a debate within the EIT community about the meaning of heart-frequency EIT signals (Adler and Boyle, 2017; Frerichs *et al.*, 2017). Not all perfusion results in a cardiac-frequency change (for example, continuous blood flow in capillaries), and non-perfusion effects (for example, heart movement in the thoracic cavity) can result in heart-frequency EIT signals. This debate is reflected by the terminology – perfusion vs. pulsatility. Those who prefer "pulsatility" or "heart-frequency fEIT image" seek to emphasise that frequency filtered signals are not "perfusion" (although they may be related). While these pulsatility based EIT images are clearly not a direct measure of perfusion, the signals appear to be useful and are often measured and reported (Bartocci *et al.*, 1999; Ericsson *et al.*, 2016; Halter *et al.*, 2008; Moens *et al.*, 2014). To the authors' knowledge, no systematic comparison of frequency-based perfusion measures has been published.

The heart-frequency signal can be derived from frequency filtering or ensemble averaging. Frequency-filtering uses a filter to isolate the frequency of heart-frequency conductivity changes, and was introduced by Zadehkoochak *et al.* (1992) and Leathard *et al.* (1994). Frequency filtering is susceptible to interference from ventilation when the heart rate is at a harmonic of the breathing rate. Ensemble averaging is another filtering approach which averages signals at a synchronized time, for example at the QRS peak (Bartocci *et al.*, 1999; Deibele *et al.*, 2008). The impedance change due to each heart beat is aligned and averaged to give a single heart-related impedance change, representative of all heart-beats in the segment.

In this paper, we are motivated to better understand the relationship between lung perfusion and heart-frequency filtering measures, and between the various fil-

tering approaches used to determine heart-frequency components. Our questions are: 1) to what extent do heart-frequency filtering-based measures correspond to perfusion, 2) what are the advantages and disadvantages of different approaches to heart-frequency filtering of EIT data, and 3) which techniques are recommended. In our experimental protocol, we have selected posture-change to introduce changes in the regional distribution of lung perfusion. These changes are then compared using bolus- and filtering-based EIT measures.

3.2 Methods

3.2.1 Overview

Data were acquired as an additional protocol within a study to determine a baseline for lung damage due to gas ventilation in neonatal lambs. This is part of an effort to establish total liquid ventilation (TLV) as a less-injurious ventilation strategy for the delicate lungs of neonatal subjects (Sage *et al.*, 2018). In order to induce changes in ventilation and perfusion patterns, posture changes were made between supine, prone, left and right lateral positions.

3.2.2 Animals

The study was conducted in accordance with the Canadian Council on Animal Care guidelines upon approval by the animal research ethics board of Université de Sherbrooke (protocol 417-17BR).

Seven healthy neonatal lambs (2–4 days old and 2.95±0.27 kg) were used. An-

imals were anaesthetised (ketamin 10 mg/kg IM at induction followed by propofol 100 mcg/kg/min and ketamin 2 mg/kg/h IV) and placed under mechanical gas ventilation with: peak inspiratory pressure (PIP) 15 cmH_2O, positive end-expiratory pressure (PEEP) 5 cmH_2O, respiratory rate (RR) of 60/min, and fractional concentration of O_2 in inspired gas (FiO_2) of 30%.

A catheter was inserted into the carotid artery for blood gas and continuous blood pressure monitoring. A jugular venous access was inserted to inject the saline bolus for generating perfusion images. Each animal was shaved for placement of a custom EIT belt around the lower third of the sternum in the transverse plane.

For each animal a bolus injection protocol was used: 1.5 mL of 7.5% saline was injected into the jugular vein at a constant rate over approximately 2s. Before each bolus, ventilation was stopped for ten seconds, and a further twenty seconds of apnoea was maintained before restarting ventilation.

After one hour of ventilation (for stabilization) EIT recordings were made during the position change procedure. Each lamb was rotated onto its right side. Five minutes after turning the subject, the bolus injection protocol was implemented. The animal was then ventilated normally, remaining on the right side for an additional five minutes, before being positioned on the left side for 5 minutes of regular ventilation, followed by the bolus injection protocol.

At 2 hours of ventilation, the position change procedure was repeated, changing the positioning of the lamb from prone to supine as the bolus injection protocol was repeated and EIT recordings were captured.

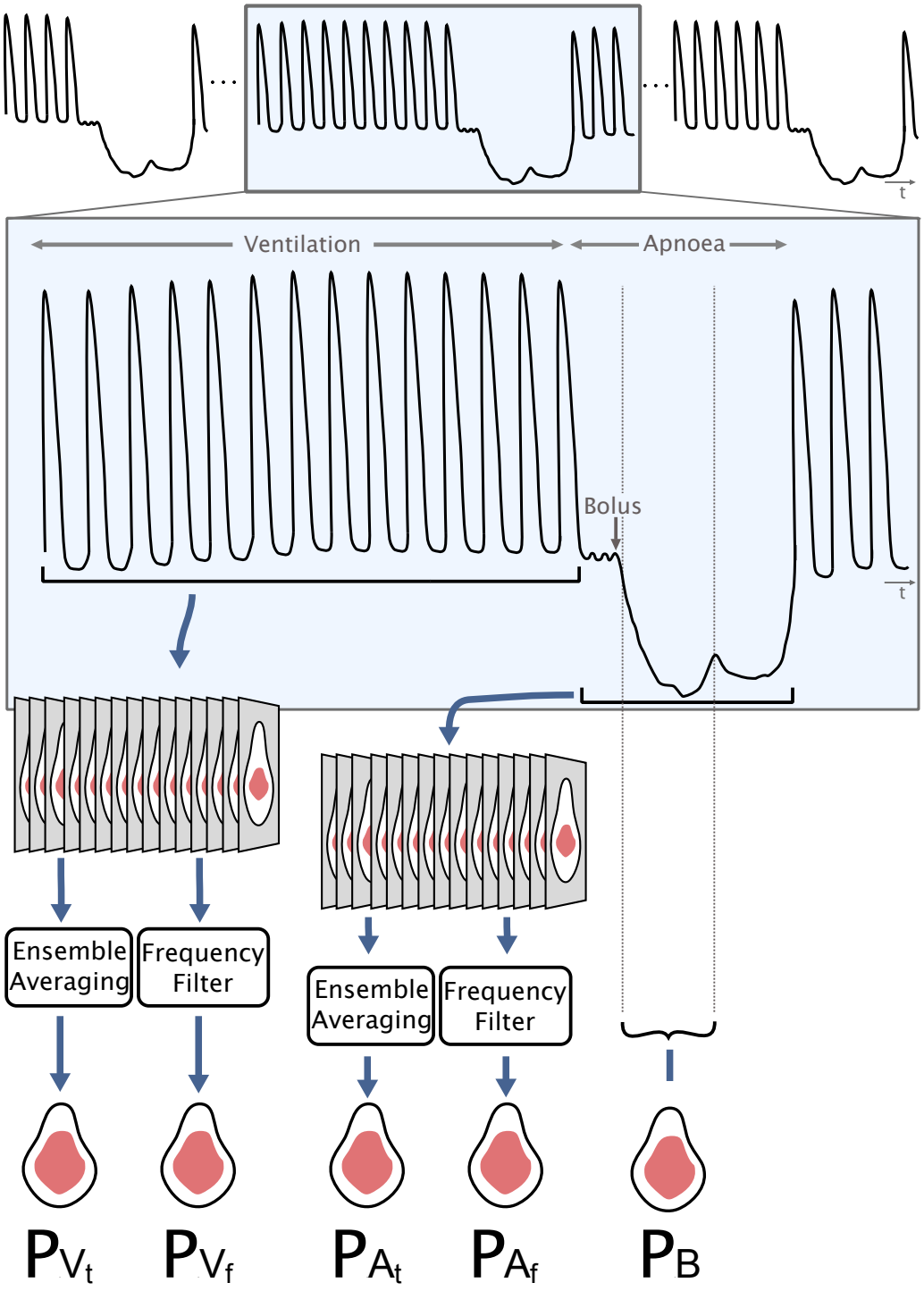

Figure 3.1: This figure is a schematic overview of analysis methods for EIT perfusion. The upper curve illustrates the global EIT signal during a period of ventilation followed by apnoea and renewed ventilation. During apnoea a bolus of conductivity contrasting saline is introduced. From these data 5 fEIT images are calculated: P_{Vt}: pulsatility (perfusion) image during ventilation, calculated by ensemble averaging EIT data during ventilation; P_{Vf}: pulsatility (perfusion) image during ventilation, calculated by frequency filtering EIT data during ventilation; P_{At}: pulsatility (perfusion) image during apnoea, calculated by ensemble averaging EIT data during apnoea; P_{Af}: pulsatility (perfusion) image during apnoea, calculated by frequency filtering EIT data during apnoea; P_B: perfusion image from bolus, calculated between a reference measure during apnoea and one during the bolus

3.2.3 Data Acquisition and Image Reconstruction

EIT data was acquired with the Pioneer Set (Swisstom, Landquart, Switzerland) using a custom electrode belt (at an acquisition rate of 20 frames/s). The belt uses 32 brass electrodes equally spaced around the thorax, using an ultrasound gel to ensure good contact and minimise the contact impedance. The selected data in this study comes from lateral positioning changes recorded after after 1.5 hours of ventilation and prone to supine positioning changes after 2 hours.

EIT images were reconstructed using GREIT (Adler *et al.*, 2009), which calculates a reconstruction matrix $\mathbf{R}$ from which the reconstructed image is calculated as $\hat{\mathbf{x}} = \mathbf{R}\mathbf{y}$, where $\mathbf{y}$ are the time-difference measurements, $\mathbf{y}(t) = \mathbf{v}(t) - \mathbf{v}(t_r)$, where $\mathbf{v}(t)$ represents the data frame acquired at time, t, and $\mathbf{v}(t_r)$ measurements acquired at a "reference" time, t_r in the case of this experiment the reference was a mean of 10 images preceding the bolus injection.

The linear reconstruction matrix $\mathbf{R} = \mathbf{D}\boldsymbol{\Sigma}_t\mathbf{J}^T\left(\mathbf{J}\boldsymbol{\Sigma}_t\mathbf{J} + \boldsymbol{\Sigma}_n\right)^{-1}$ is calculated from a finite element model of the body and electrode geometry $F(\cdot)$ and covariance estimates of the image, $\boldsymbol{\Sigma}_t$, noise, $\boldsymbol{\Sigma}_n$ (Grychtol *et al.*, 2016), and a spatial filtering matrix, $\mathbf{D}$.

EIT data from this experiment was prone to errors consisting of brief periods of zeroed measurements stemming from the synchronisation equipment. Measurements that were zeroed by the device were removed and replaced with linearly extrapolated data to allow for frequency-based analysis over all selected segments of data. A moving median filter with a width of 3 was used to further remove the noise caused by single measurement errors in the signal.

3.2.4 Functional EIT Images

In each animal 4 episodes were recorded — one in each posture — to generate 5 different functional EIT images.

The images Bolus-based measures of lung perfusion (P_B) were calculated using time-difference reconstructions. Heart-frequency filtering during ventilation (P_{Vf}) and apnoea (P_{Af}) used frequency analysis of EIT image sequences, as illustrated in figure 3.3, and ensemble averaging-based methods during ventilation P_{Vt} and apnoea P_{At} are calculated using ensemble averaging of identified pulsitile components figure 3.4.

The following methods were conducted on segments of data collected both during apnoea and ventilation. Apnoea regions were selected as the total time that ventilation was arrested, including the bolus section and had a duration of 30s. The ventilation data was selected as 30s of data immediately preceding the induction of apnoea. Regions of interest including lung, and heart areas in the images were defined by the lamb model provided in EIDORS (Adler *et al.*, 2017a).

3.2.4.1 Bolus injection image (P_B)

The beginning of the saline bolus injection was determined as the point immediately preceding the drop in impedance from the conductive agent, and is shown in figure 3.2 at the point marked “injection”. The mean of 10 images including and immediately preceding the bolus injection were used as the reference to which all bolus images were reconstructed from. To image perfusion, the point with maximum decline in impedance over the sum of the pixels in the lung region relative to the reference was

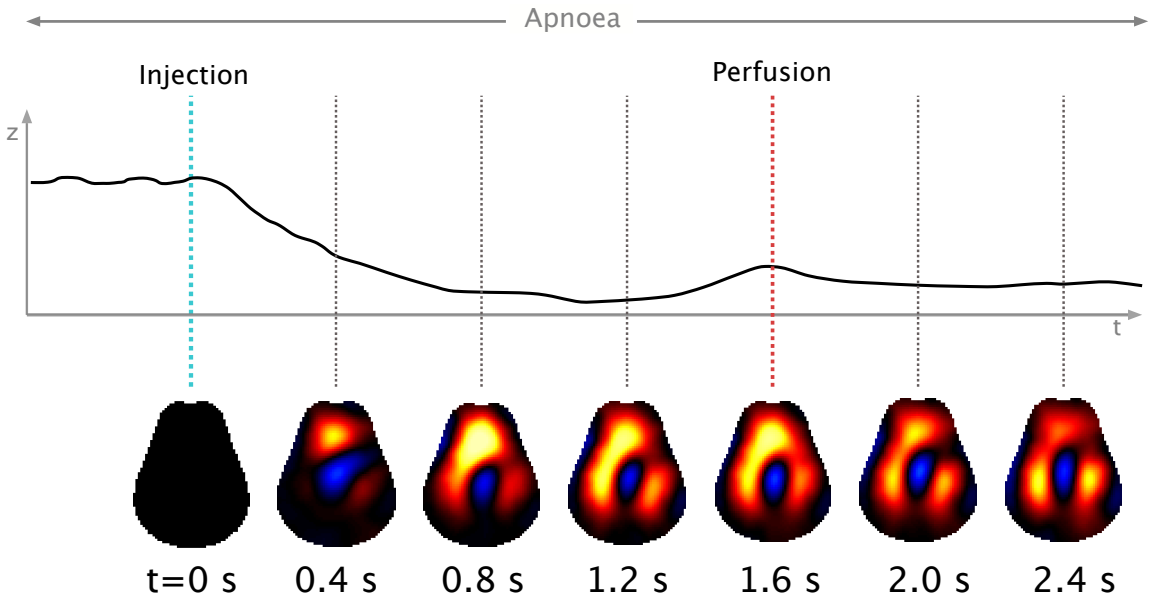

Figure 3.2: The method used to select the perfusion point from the bolus injection is shown in the figure above. The point with the widest spread of high conductivity was selected as the point of perfusion, shown here at 1.6 seconds after the contrast agent injection. The image series shows the conductivity contrast as the bolus injection travels through the thorax.

selected based on the methods presented by Frerichs *et al.* (2002). In figure 3.2 this was found at the point marked "perfusion". This method was used as the standard perfusion measuring technique against which the other methods were compared.

3.2.4.2 Frequency-Filtering

Heart-frequency EIT images during the selected events were calculated by taking the FFT of the time-series image data after first applying a Blackman window: $w(n) = a_0 - a_1 \cos\left(\frac{2\pi n}{N-1}\right) + a_2 \cos\left(\frac{4\pi n}{N-1}\right)$ with $a_0 = 0.42$, $a_1 = 0.5$ and $a_2 = 0.08$, where N is the number of time-series EIT images in the selected event.

An FFT was calculated from a series of images restricted to pixels in the heart

region. From the FFT of all pixels the heart region, the heart frequency was selected as the largest peak between 3 and 4.5 Hz, representing a heart rate between 180 and 240 bpm (typical for a newborn lamb).

The identified heart rate was used to select changes at the heart-frequency in the frequency domain images of the entire thorax. Images at 3 frequencies on either side of the heart rate were also reconstructed to account for changed in heart rate over the course of the data collection. A Blackman window with a length of 7 was applied surrounding the heart frequency to generate a weighted mean of the images, resulting in a single perfusion image from the heart-frequency data.

The output of the frequency filtering method is an image with complex values assigned to each pixel.

Depending on the timing of the pulsatility-based changes within the selected signal the real component of frequency analysed image did not correspond to the maximum conductivity change in the lungs in every event. In order to correct this, each image was displayed along the axis that gave the maximum real component contained within the lung region to ensure the maximum change in impedance related to pulsatile activity in the lungs was calculated.

3.2.4.3 Ensemble Averaging

Time series data of the total impedance signal for each pixel in the heart region was filtered using a bandpass filter to eliminate noise and breathing changes, and allow the heartbeat to be seen clearly in the signal. Peak detection was used on this heart-region data to select the amplitude peaks in impedance change signal at the

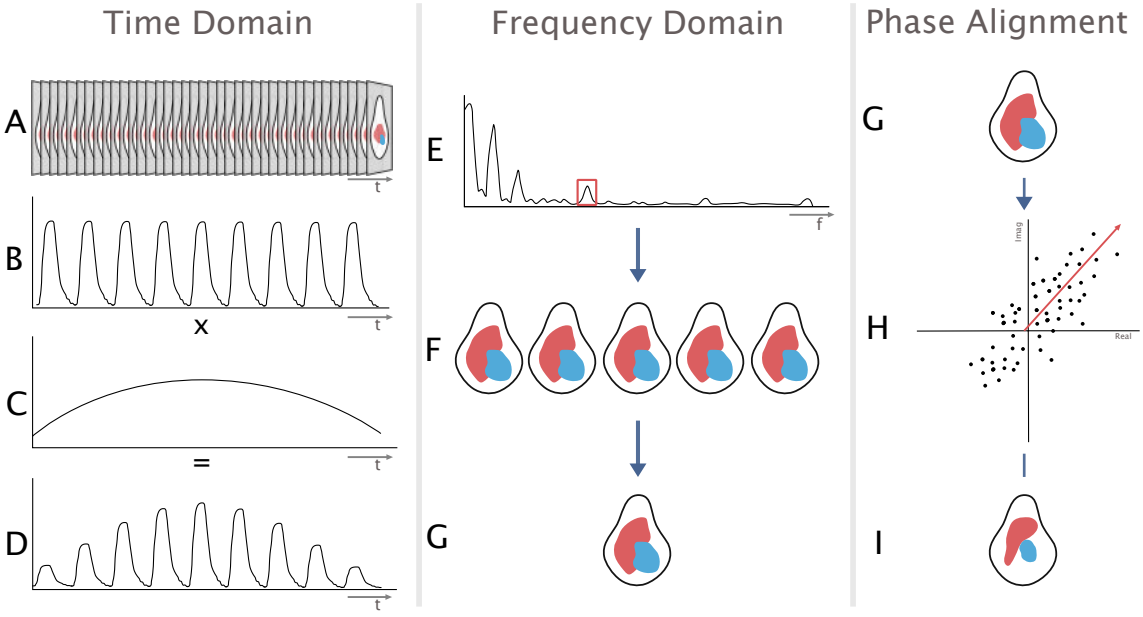

Figure 3.3: Frequency analysis methodology used for obtaining a perfusion image from the time series data. Steps are: A) to reconstruct the images from time series measurements; B) - D) window the time series data before performing a FFT on the data for each element; E) Select the dominant frequency between 3 and 4.5 Hz as the heart frequency; F) reconstruct the image at the heart frequency and selected nearby frequencies; G) take the mean of the images at the heart frequency using a Blackman window to give greater weight to those closer to the center; H) I) select the image that will give the maximum real component contained in the lung region.

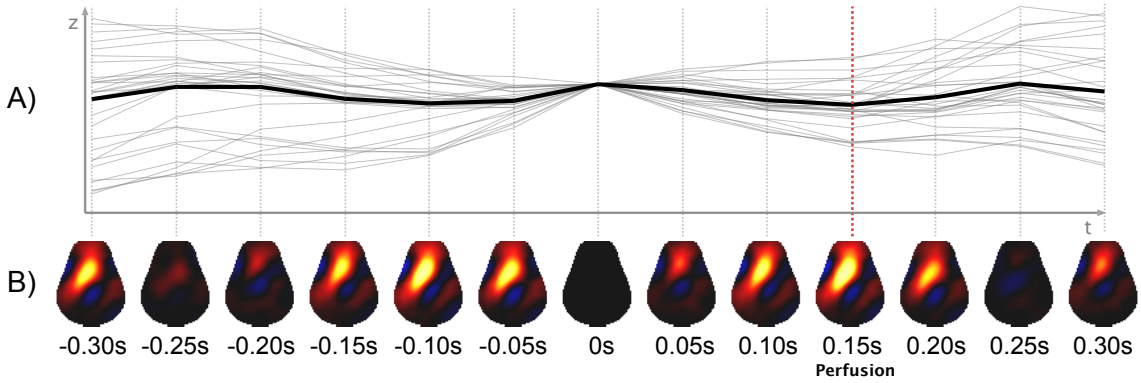

Figure 3.4: Illustration of the stages of the ensemble averaging process: A) an ensemble average of all heartbeats over the time frame is taken from the summed global signal; and B) shows reconstructed images corresponding to each time point in the global ensemble averaged signal above. The selected perfusion image is the image with the maximum impedance increase in the lung region.

heart frequency.

Using the identified time points, the global impedance change signal was ensemble averaged by overlaying all identified peaks to give an averaged heartbeat. 13 images were reconstructed over the course of the heart beat to select the image that resulted in the maximum positive increase impedance within the lung region. This process is outlined in figure 3.4.

3.2.5 Image Comparison

To compare the images the Jaccard distance between functional EIT images was calculated. Negative impedance changes were removed from the images and the images were normalized.

The Jaccard distance was calculated between the reference image calculated using the maximum increase in lung-region conductivity during bolus injection (b), and

the frequency-based method (f): $J(x,y) = \sum_i \frac{min(b_i,f_i)}{max(b_i,f_i)}$ representing the distance between the two images.

3.2.6 Statistical Analysis

To determine the significance of the change in bolus between postures and methods, the Cohen's d score was calculated to quantify the effect size of the change in the centre of mass of the perfusion image (Cohen, 1977). This was calculated as the difference between two means over the pooled standard deviation. Where the difference between the two means is: $\mu_1 - \mu_2$, and the pooled standard deviation is: $\sqrt{\frac{(n_1-1)s_1^2+(n_2-1)n_2s_1^2}{n_1+n_2-2}}$.

3.3 Results

The Jaccard scores for each method were compared between ensemble averaging and frequency filtering methods to determine the regions where performance was best for each method. Figure 3.5 shows a comparison between Jaccard distance for each animal, connecting lines indicate different methods performed on the same data segment, while each marker shape denotes a separate posture.

On average frequency filtering outperforms ensemble averaging based methods of perfusion calculation (p=0.04), and there is no significant difference in performance of the heart-frequency based filtering techniques during periods of apnoea relative to periods of ventilation.

Of the 56 data regions that were analysed, the ensemble averaging performed bet-

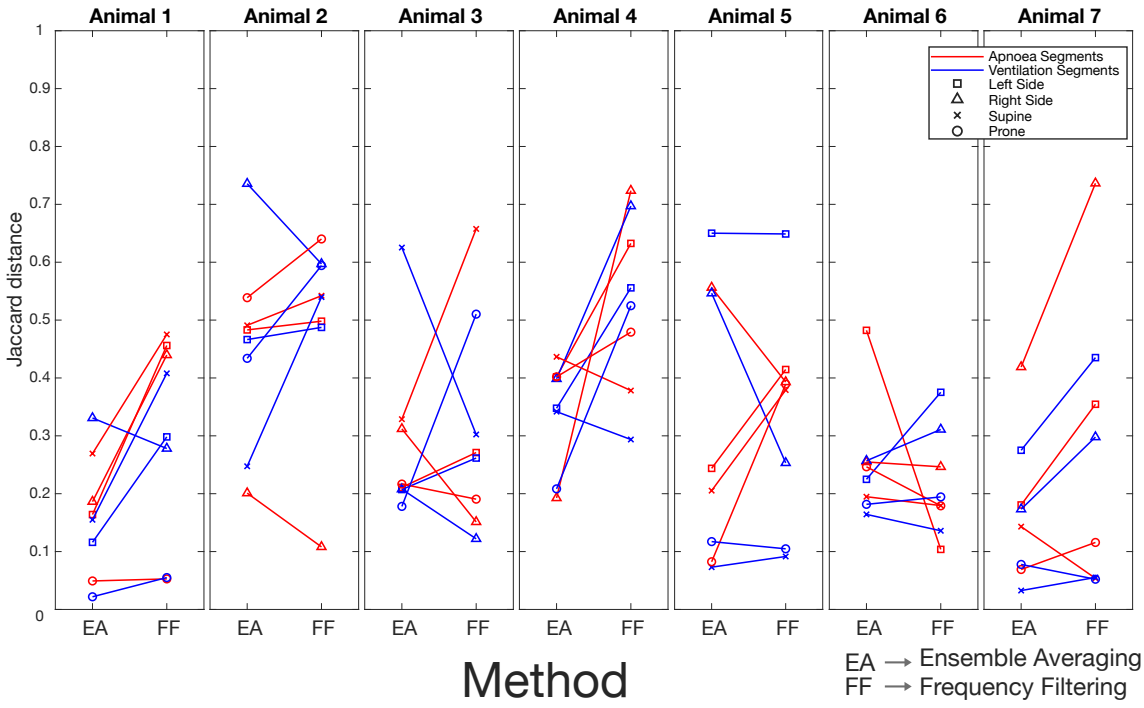

Figure 3.5: Jaccard scores for each method and animal in the comparison. Frequency filtering and ensemble averaging methods performed on the same data segment are connected by solid lines. Red lines and markers indicate apnoea data sections, while blue indicates ventilation data sections. Each posture is denoted by a different shaped marker in the figure.

ter in 12 cases and the frequency filtering achieved the best performance in 28 cases, there, were 16 additional cases where the difference in performance was negligible at less than 5%. On average, across all images, frequency filtering based methods scored 7% higher than ensemble averaging.

The center of mass of the perfusion measure images using the bolus injection method had a Cohen's d score of less than 0.1 between posture changes indicating that there is an insignificant or trivial difference in the means relative to the standard deviation (Cohen, 1977). To demonstrate the visually observable changes due to posture change and the high similarities that can be observed between filtering- and bolus-based perfusion estimates, frequency filtered images from animal 4 are compared to bolus based methods in figure 3.6.

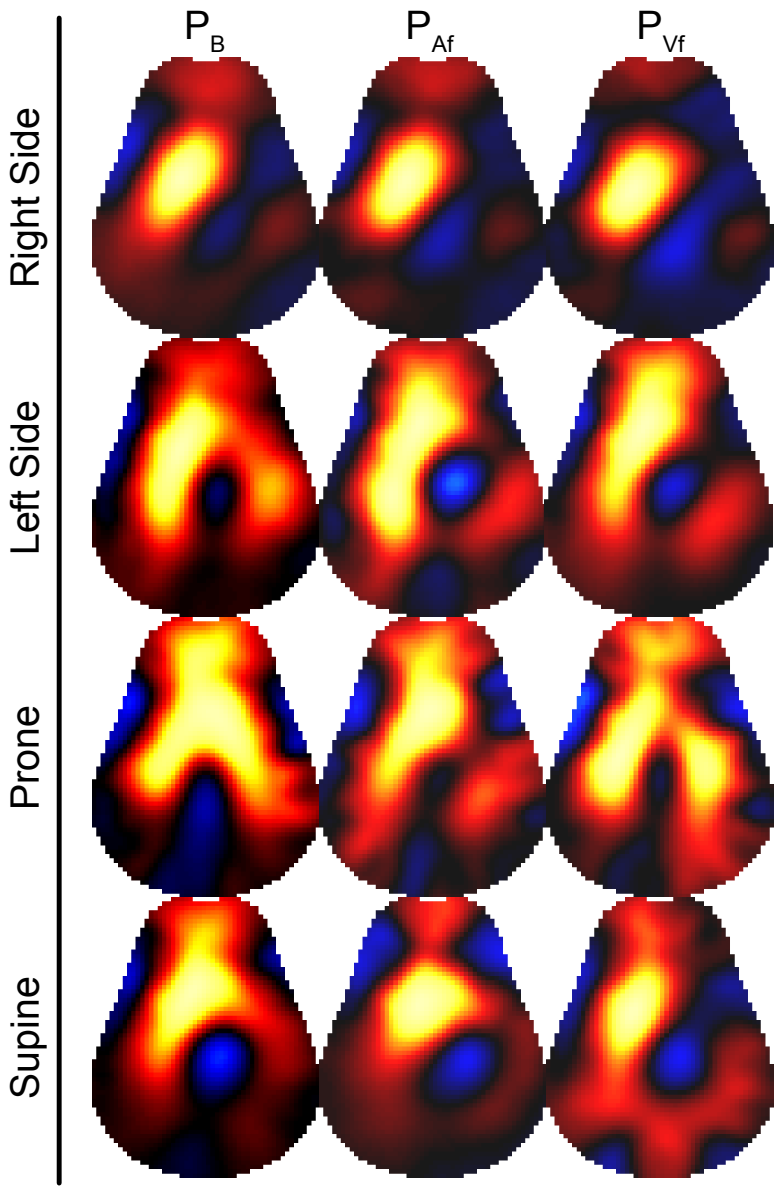

Figure 3.6: This figure shows the tracking of perfusion for frequency filtering measures of perfusion during apnoea and ventilation sections compared to bolus injection for animal 4. P_B is the bolus injection image, P_{Af} uses the frequency filtering method during apnoea and P_{Vf} is the frequency filtering method during ventilation.

3.4 Discussion

Two primary approaches of EIT perfusion calculation have been compared in this paper: injection of a bolus of contrast-agent resulting in EIT image changes which produce perfusion measures, and digital filtering of EIT image sequences to extract the heart-frequency components. Additionally, various algorithms have been evaluated for digital filtering-base approaches during mechanical ventilation and short apnoea sequences, using both frequency- and ensemble averaging-based techniques. There have been few comparisons of these techniques, and we set out to better understand the relationship between perfusion and heart-frequency measures, and between the various filtering approaches used to determine heart-frequency cardiac changes. We selected an experimental protocol using posture-change to alter the regional distribution of lung ventilation and perfusion in newborn lambs.

Our first question was "to what extent do heart-frequency filtering-based measures correspond to perfusion?"

The primary results (figure 3.5) use a Jaccard index of the similarity between functional images. Overall it was found that in healthy animals the Jaccard index indicated good agreement with our gold standard. While highly dependant on the data, it was found that there was a high degree of similarity between methods with respect to the overall shape of the perfusion. In both animals 2 and 4, where the signal required little preprocessing before analysis there is a higher Jaccard score across all cases.

The synchronisation box was attached to the EIT system but was not used for this experiment, an error in the connection caused brief periods of the signal (less

than 1 s) in some animals to be zeroed. Through careful processing of this signal only brief sections of data were lost and we do not feel this impacts the results.

During the experiment the order of posture change was not randomised. While changes in ventilation due to posture change are not understood to have long term physiological effects, if there is a longer term effect of change in posture the lack of randomisation will impact the results. Nguyen *et al.* (2015) were able to image perfusion changes due to induced pulmonary embolisms and using the peak impedance change on dilution curves, however our data presented insufficient variance in perfusion induced by posture change to complete a center of mass analysis. A higher statistical power could potentially be achieved through initiating posture changes with more dramatic results in perfusion, such as upright to supine (Nakazato *et al.*, 2010).

Throughout the experiment, the perfusion image was selected as the image containing the largest increase in conductivity in the sum of pixels in the lung region, which occurred at different relative times across animals and events. Many factors could affect this including belt positioning changes, and it could be a contributing factor to the inconsistent trends in amplitude changes in the global image across methods. Borges *et al.* (2012) compared EIT perfusion images using first-pass kinetics and heart-frequency filtering based methods to perfusion measures using SPECT, finding that heart-frequency filtering techniques made systemic errors when used to estimate the perfusion. They also determined that there was no discernible relationship between the magnitude of the SPECT images and the heart-frequency images. This was consistent with the findings of this study that image amplitude

of the bolus injection and heart-frequency filtering-based methods was not consistent in all animals. This methodology presented by Borges *et al.* (2012) was not part of the comparison in this study as the edentification of the perfusion signal due to the heart could not be consistently identified and removed across all animals. In two dimensions, heart-frequency and ventilation signals have been used to identify the location of the heart and lungs within the EIT electrode plane with known electrode locations and anatomy (Ferrario *et al.*, 2012), but in situations where the electrode location and anatomy is not precisely known EIT tends to perform poorly as a structural imaging modality (Adler and Boyle, 2017). These challenges suggest that configurations with multiple planes of electrodes may be better able to isolate and remove off-plane pulsatility signals related to the heart.

It was observed that the general shape of the perfusion was consistent across all methods despite amplitude variations. One reason for the difference in amplitude change across animals may be due to slight variations in the belt placement and electrode positioning on the animals. If the belt is closer to the heart, there will be a larger heart-frequency component to the signal and there may be a variance in the impedance change due to bolus injection.

Next, we asked "what are the advantages and disadvantages of different approaches to heart-frequency filtering of EIT data, and which techniques are recommended under which circumstances?"

Our overall recommendation is that, whenever possible, frequency filtering techniques should be used. This is largely because frequency filtering methods tend to be more stable in the presence of noise on the signal. Ensemble techniques are

advantageous in some circumstances, because they better use the heart-frequency variability to avoid interference from harmonics of the ventilation at the heart rate. For frequency-filtering techniques, it is necessary to widen the heart-frequency filters to account for such variability. On the other hand, it is sometimes not possible to accurately synchronize heartbeats, due to noise corruption in the signals or the very low amplitude of the heart-frequency signals relative to the ventilation signal. In cases where the signal of the heartbeat was not clearly identifiable through visual inspection of the signal, neither ensemble averaging nor frequency filtering was able to achieve good estimates of perfusion relative to the bolus injection event.

In summary, our goal was to understand the relationship between bolus- and filtering-based EIT measurements of lung perfusion, as well as the relationship between different filtering-based measures of perfusion. Our results indicate there is a common trend between the shape and perfusion estimates of both heart-frequency and bolus injection images despite the difference in physiological events behind each measure. Amongst filtering techniques, frequency filtering outperforms ensemble averaging across regions of data where there is noise present and the heart signal cannot be readily identified, and both methods were able to approximate the bolus injection measures equally well when applied to apnoea and ventilation regions of data.

3.5 Summary

Two main functional imaging approaches have been used to measure regional lung perfusion using Electrical Impedance Tomography (EIT): venous injection of a hy-

pertonic saline contrast agent and imaging of its passage through the heart and lungs, and digital filtering of heart-frequency impedance changes over sequences of EIT images. This paper systematically compares filtering-based perfusion estimates and bolus injection methods to determine to which degree they are related. EIT data was recorded on 7 mechanically ventilated newborn lambs in which ventilation distribution was varied through changes in posture between prone, supine, left- and right-lateral positions. Perfusion images were calculated using frequency filtering and ensemble averaging during both ventilation and apnoea time segments for each posture to compare against contrast agent-based methods using Jaccard distance score. Using bolus-based EIT measures of lung perfusion as the reference frequency filtering techniques performed better than ensemble averaging and both techniques performed equally well across apnoea and ventilation data segments. Our results indicate the potential for use of filtering-based EIT measures of heart-frequency activity as a non-invasive proxy for contrast agent injection-based measures of lung perfusion.

Chapter 4

FEM mesh refinement for 3D EIT

4.1 Motivation

This thesis proposes the use of novel 3D electrode configurations and internal electrodes to improve sensitivity to cardiosynchronous activity. Unlike surface electrode configurations, these modles will have a very high sensitivity in the center of a model where mesh refinement can be challenging. In this chapter we explore the need for mesh refinement with regard to sensitivity accuracy.

4.2 Introduction

Electrical Impedance Tomography (EIT) reconstructs images of electrical tissue properties within a body from electrical transfer impedance measurements at surface electrodes. For biomedical imaging applications, it is being actively studied for monitoring the movement of air and blood in the thorax, and for imaging the head and

breast. Reconstruction of EIT images requires the solution of an inverse problem in soft field tomography. EIT image reconstruction requires calculation of a sensitivity matrix, **J**, representing the relationship between internal changes and measurements. A pseudo-inverse of **J** is used to update the image estimate over several iterations. EIT image reconstruction is ill-posed, since the physics of current propagation implies that sensitivity is largest near the electrodes and smallest in the body centre.

It is therefore clear that a precise calculation of **J** is required for solution accuracy. Since it is generally not possible to use analytic solutions, because of the non-regular shapes of biological bodies and the boundary conditions on a conductive electrode, the finite element method (FEM) is typically used. One key advantage of the FEM is that element size can be selectively refined in regions to meet solution accuracy. The accuracy of the FEM solution will increase as more elements are added, so a high mesh density is often desired to achieve an accurate solution. In this paper we will use the term mesh to refer to a specific combination of nodes and elements in a finite element model. In EIT the sensitivity is nonuniform across the entire model. Thus it has generally been recommended in the EIT literature that meshes be refined near electrodes, where the electric field and sensitivity are largest (Adler and Boyle, 2017). This recommendation gives rise to two questions: 1) No thorough analysis has been made to determine how much refinement is required. Given a "mesh element budget", what should balance of nodes be between the centre of the model and the electrodes? And 2) How do different freely available meshing tools that are commonly used with EIT compare when used to refine 3D meshes?

Previously with EIT, mesh refinement has primarily been either constant, or

based on the complexity of geometric surfaces and lines within a model (Grychtol and Adler, 2013). In EIDORS (Adler and Lionheart, 2006) meshes are generated using both Netgen (Schöberl, 1997) and Gmsh (Geuzaine and Remacle, 2009) for 2D and 3D models. Refinement around electrodes is commonly performed by setting a mesh density for the electrodes and allowing the mesh density to decay towards the maximum mesh size. This does not allow the user to specify the rate of decay or precisely control the mesh size.

A model that accurately represents the anatomy of the imaged region can greatly increase the quality of the reconstructed image (Grychtol *et al.*, 2012), but increasing the complexity of mesh surfaces presents additional challenges for mesh refinement. EIT reconstruction software EIDORS enables users to place electrodes on the surface of complex boundaries (Grychtol and Adler, 2013), but the current functionality does not enable control of the refinement around the electrodes or internal structures. Most commercially available FEM packages do not conveniently provide such capability either.

In this paper we investigate approaches to manage the tradeoff between refinement of the electrode regions versus the bulk volume. We present a comparison between Gmsh and Netgen based mesh refinement around electrodes, and evaluate the effect of mesh refinement techniques on error in the sensitivity matrix, $\mathbf{J}$.

4.3 METHODS

4.3.1 Overview

We built a cylindrical model in Gmsh and Netgen which was parameterized so that multiple different combinations of mesh refinement were possible. These results were compared to a very high density meshes which was considered the gold standard. The format of the geometry files used to generate these meshes can be seen in appendix A.

4.3.2 Mesh Generation

A cylinder ($\varnothing = 0.5$ m, height $h = 0.25$ m) with four square electrodes (5 cm edge length) placed equidistantly around the perimeter at mid-height was meshed with Netgen (version 5.3.1) (Schöberl, 1997) and Gmsh (version 4.7.0) (Geuzaine and Remacle, 2009) meshing software. Current was injected between adjacent electrodes and the voltage was measured between the remaining two electrodes. For 3D meshes an initial analysis was done building on work from Grychtol and Adler (Grychtol and Adler, 2013) where mesh density was set by specifying the maximum edge lengths permitted on electrode surfaces and in the volume of the FEM. Results were compared against those generated using ultra-fine meshes. Calculations were performed with EIDORS (version 3.10) (Adler and Lionheart, 2006) in Matlab 2019b (The Mathworks, Natick, MA, USA).

Meshes of different sizes were generated with Netgen and Gmsh by manipulating the desired maximum edge length (maxh parameter) for the entire domain and the electrodes. Two mesh analyses were performed. For the first mesh, maximum ele-

ment lengths were chosen such as to divide the electrode side of 5 cm into an integer number of segments of equal size. The maximum mesh element length ranged from 1 to 7 subdivisions of the electrode edge, while the maximum mesh element length in the ultra-fine reference mesh was 15 subdivisions per electrode edge. Independent reference meshes were generated for each software. Two types of models were generated this way. Constant models C1–C7, where the mesh size was constant, and refined models R1–R7 where the electrode mesh size was specified and dissipated towards an internal mesh element size of 5 cm. Additional refined meshes were generated with reduced mesh size in the internal mesh regions. R1-R7 is referred to as refinement A where the internal element max size was 5 cm. Refinement B had an internal mesh size of 4 cm, C was 3 cm and D was 2 cm. The numeric value in the mesh ID indicated the number of subdivisions per electrode edge. In Netgen the mesh decay was not easily controlledbeyone selecting a refinement level from 1 to 5, but in Gmsh the size was set to increase evenly from the surface of the electrode to the centre of the model. It should be possible to replicate this mesh density distributionin Netgen by using a seperate mesh density file that specifies the required density at each point in the geometry, but this technique is not widely used due to its complexity. Figure 4.1 shows example meshes of coarse, fine and refined meshes. Figure 4.2 shows the generated mesh structure for constant refinement meshes around the electrode for both Netgen and Gmsh.

For the second analysis, the distribution of nodes within the model was changed without altering the total number of nodes to give M1 – M17. Starting with the constant mesh C3 as M1, the maximum mesh element length on the electrode was

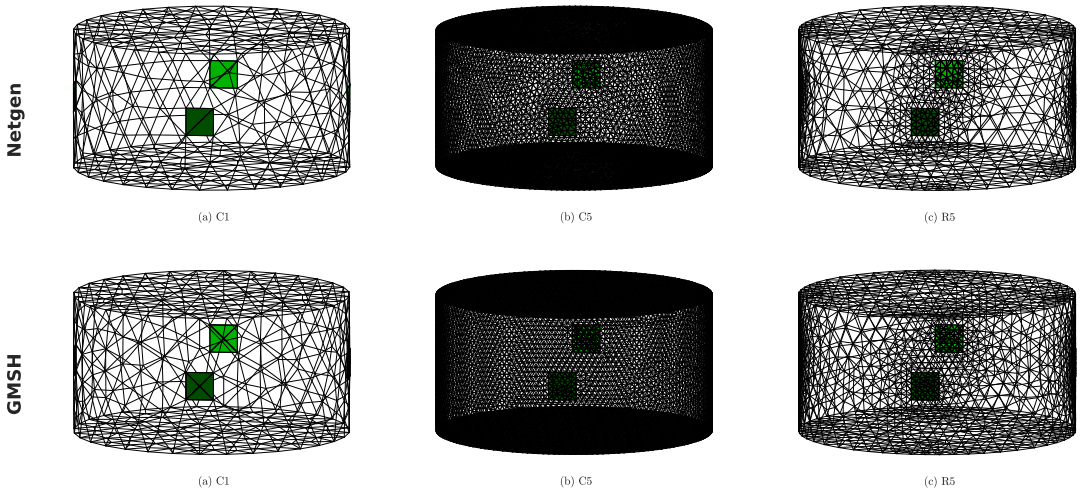

Figure 4.1: Sample meshes generated with Netgen (top row) and Gmsh (bottom row). From left to right: (C1) the coarsest constant mesh; (C5) a refined constant mesh; and (R5) a refined mesh with the same electrode mesh density as C5 but lower internal mesh density.

decreased by 10% and the maximum mesh size in the centre was increased so that the total number of elements in the mesh was within 10% of the original mesh. C3 was chosen as the starting point because several steps of mesh refinement could be generated before the electrode mesh density surpassed the reference meshes. For mesh M17 the specified electrode refinement was equal to the reference mesh. In Netgen the mesh dissipation rate was not further controlled, and in Gmsh the mesh density decreased evenly from the electrode surface to the centre of the model. To compare these meshes a section of the model was selected encompassing all points between the centre of the model and a selected electrode face. The average distance, or balance point, along the x-axis of the selected points was expressed as a percentage of the tank radius. This process is illustrated in figure 4.3.

When generating meshes to compare across several mesh density profiles as the

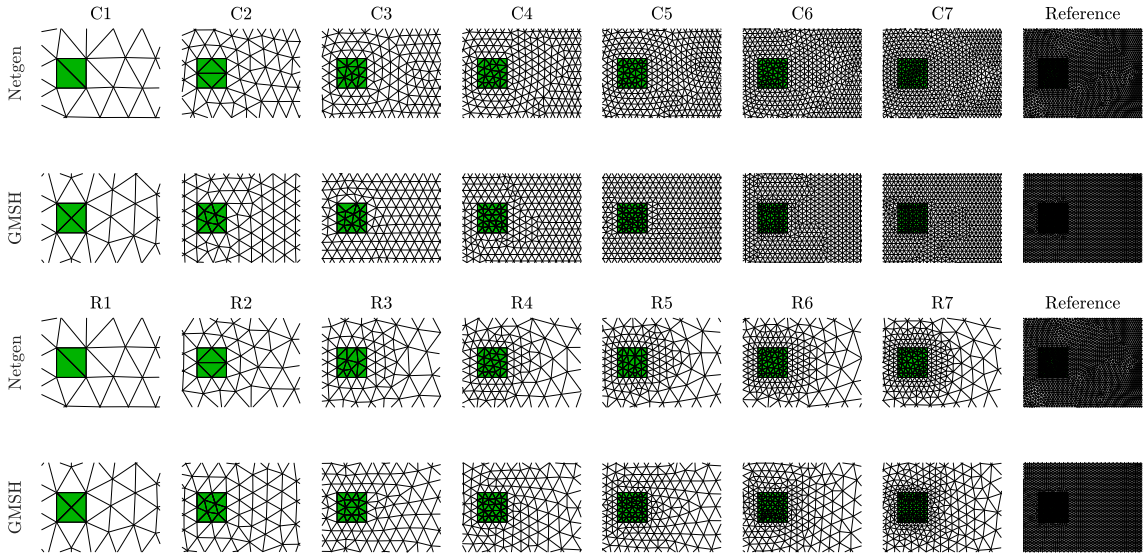

Figure 4.2: A view of the electrode meshing for all constant-density meshes in Netgen and Gmsh. The top two rows show all electrode faces and immediate surrounding surroundings from coarsest (C1) to finest (C7). C represents the constant mesh refinement and the number represents the specified mesh subdivisions per electrode edge. The reference mesh is equivalent to C15. The bottom two rows show refined meshes R1 to R7 with both Netgen and Gmsh and shows the rate of mesh dissipation away from the electrodes.

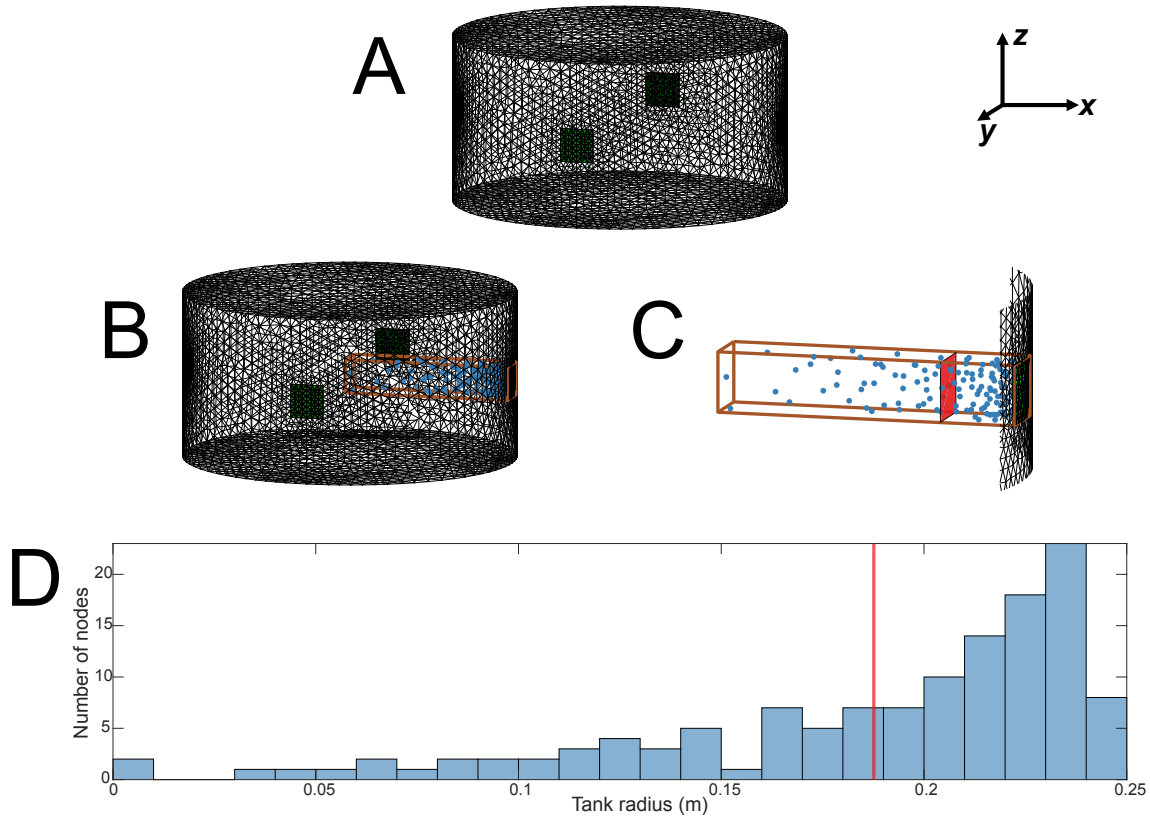

Figure 4.3: A sketch of the process to determine the balance point of generated meshes. A) the starting mesh; B) nodes between the electrode surface and the centre of the model are identified; C) the balance point of the nodes along the x-axis is calculated and indicated by the red plane; D) a histogram showing an example distribution and balance point (red) for the selected model.

balance of the nodes was shifted towards the electrodes, 19 meshes were generated for each software including 2 reference meshes. table 4.1 shows the parameters of the resulting odd numbered meshes.

4.3.3 Simulation

The potential at each node $\mathbf{V}$ of the mesh was calculated using the finite element method (FEM) using the linearization

$$\mathbf{V} = \mathbf{Y}^{-1}\mathbf{C} \tag{4.1}$$

where $\mathbf{Y}$ is the admittance matrix of the FEM (and a function of conductivity distribution) and $\mathbf{C}$ is a matrix representing the current injection pattern, such that $\mathbf{C}_{ij}$ represents the current injected in electrode i during the j-th stimulation. Here, we drive current of 1 A between two adjacent electrodes in a single stimulation, so $C = [0\,|\,0\,|\,1\,|\,-1]^T$. We pick a node in the centre of the FEM as ground, since it is necessary to assume the potential on one node for $\mathbf{Y}$ to be invertible. We use the complete electrode model and assume contact impedance of 0.01 Ω in the calculation of the admittance matrix (Polydorides and McCann, 2002).

We calculate the sensitivity (or Jacobian) matrix $\mathbf{J}$ of measurements $\mathbf{v}$ to changes in the conductivity σ of individual elements as $\mathbf{J}_{ij} = \frac{\partial v_j}{\partial \sigma_i}$ using the adjoint method (Polydorides and McCann, 2002). Again, since we only have one measurement, $\mathbf{J}$ is in fact a vector. We construct a sensitivity image by assigning each element i of the FEM the value of $\mathbf{J}_i$ divided by the element's volume. Mean sensitivity in

Table 4.1: Mesh parameters for odd numbered meshes generated by Netgen (A) and Gmsh (B) to determine the optimal node balance. Parameters global maxh and electrode maxh refer to the specified input parameters; the remaining columns give parameters from the resulting meshes.

Mesh ID		glbl. maxh [mm]	elec. maxh [mm]	# elem.	# nodes	# elec. elem.	minEL[a] [mm]	maxEL[b] [mm]	minEV[c] [mm^3]	maxEV[d] [mm^3]
M-01	A	16.67	16.67	31347	7095	22	9.80	49.45	254.76	6851.01
	B	16.67	16.67	49210	9615	25	10.32	50.00	222.87	2898.59
M-03	A	18.33	15.00	29639	6482	22	10.75	50.41	289.80	5826.14
	B	18.33	15.00	49247	9680	40	7.36	37.11	172.78	2814.55
M-05	A	18.33	13.33	29814	6589	28	9.39	49.91	162.26	5648.41
	B	20.00	13.33	50749	9930	42	7.80	37.93	134.41	3233.59
M-07	A	18.33	11.67	30581	6723	36	8.77	47.88	141.74	6252.36
	B	21.67	11.67	53002	10429	60	6.17	40.84	63.22	4077.18
M-09	A	18.33	10.00	30690	6755	42	7.86	49.18	115.45	5496.39
	B	23.33	10.00	56237	11008	68	5.82	43.81	62.88	4962.89
M-11	A	18.33	8.33	31575	7030	74	6.05	50.99	60.06	6086.88
	B	26.67	8.33	55545	10886	96	5.51	49.72	36.84	7424.70
M-13	A	20.00	6.67	28589	6447	92	4.65	51.85	20.68	6664.11
	B	30.83	6.67	54993	10825	148	4.51	55.36	20.63	10453.90
M-15	A	21.67	5.00	27775	6245	158	3.46	52.60	11.13	9097.30
	B	36.67	5.00	55331	11000	250	3.51	61.66	7.99	15838.09
M-17	A	30.00	3.33	39116	7590	320	1.75	72.83	1.13	23783.17
	B	48.33	3.33	52947	10798	548	2.32	86.60	2.72	32287.34
REF	A	3.33	3.33	6661789	1173243	510	1.75	9.49	1.01	46.09
	B	3.33	3.33	5871464	976558	554	2.10	7.59	1.58	21.65

a: minimum mesh edge length, *b*: maximum mesh edge length
c: minimum mesh element volume, *d*: maximum mesh element volume

the plane of electrodes is then calculated by averaging the sensitivity in fifteen planes parallel to the plane of electrodes and spanning the height of 5 cm. The sensitivity was projected onto a 512×512 array and divided into regions of interest for the centre (C), at the electrode (E) and between the centre and electrode (I). The resulting sensitivity for the reference mesh calculated with Gmsh and the selected regions of interest is presented in figure 4.5.

The sensitivity error is the absolute difference in total sensetivity for the selected region with reference to the ultra-fine model.

4.3.4 Electrode refinement for arbitrary FEMs

Our approach for refinement around electrodes in Gmsh with external electrodes also allows for the refinement of arbitrary models with complex structures such as internal electrodes and tissue boundaries. A scenario depicting an approximation of a probe entering a bone with different layers of conductivity. The resulting mesh pictured in figure 4.7 highlights the ability of this technique to be used for refinement around electrodes and the control of mesh density surrounding internal structures which was previously very challenging in EIT software.

4.4 Results

Two analyses of mesh refinement were completed. The first comparing sensitivity error between meshes with constant refinement and refinement only at the electrodes, and the second comparing meshes with different levels of electrode refinement and

the same number of nodes.

When comparing constant meshes to meshes with refinement at the electrodes, sensitivity error was decreased as more nodes were added to the mesh and to the electrodes. The sensitivity error was lowest in the constant meshes across both Netgen and Gmsh software. Meshes generated using Netgen provided a slightly lower sensitivity error relative to the respective reference mesh compared to Gmsh, and resulted in meshes with fewer nodes per electrode given the same input parameters. figure 4.4 shows the sensitivity error between constant and refined meshes with respect to the number of nodes per electrode.

Example sensitivity profiles for the M-series meshes are shown in figure 4.5. The resulting sensitivity profile near the electrodes more closely matched the reference case when refinement at the electrodes was higher.

The total sensitivity error across all meshes is plotted vs. the balance point in figure 4.6. For meshes generated with Gmsh the minimum error was achieved when the node balance point was approximately 85% of the model radius corresponding to model M15-B, and for Netgen generated meshes the minimum sensitivity was achieved in model M13-A at a balance point of approximately 70%. Gmsh achieved a lower sensitivity error measured against the respective reference mesh. For meshes using Netgen refinement, the balance point did not increase evenly as the electrode density was increased and the internal density decreased. To maintain the same number of nodes within the model, Gmsh required a larger internal maxh than Netgen. Gmsh generated meshes with more nodes for the same input parameters, but generally the resulting mesh sizes were closer to those specified. The resulting

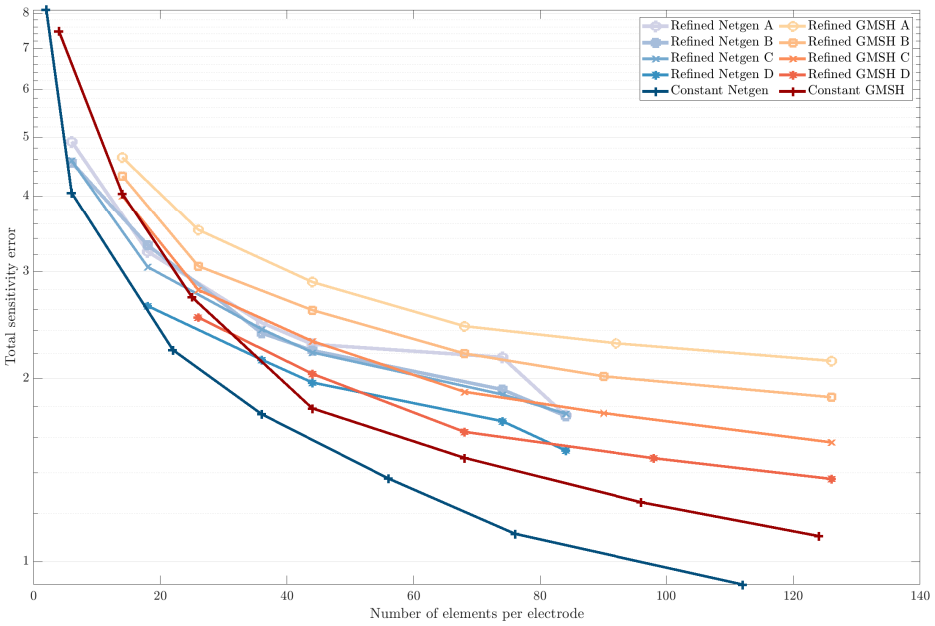

Figure 4.4: Sensitivity error of each mesh as a function of the number of elements per electrode for both Netgen and Gmsh. The darkest lines indicate the constant mesh refinement, lighter lines indicate a larger maximum internal mesh size. The maximum internal mesh sizes are as follows: refinement A - 5 cm; refinement B - 4 cm; refinement C - 3 cm; refinement D - 2 cm.

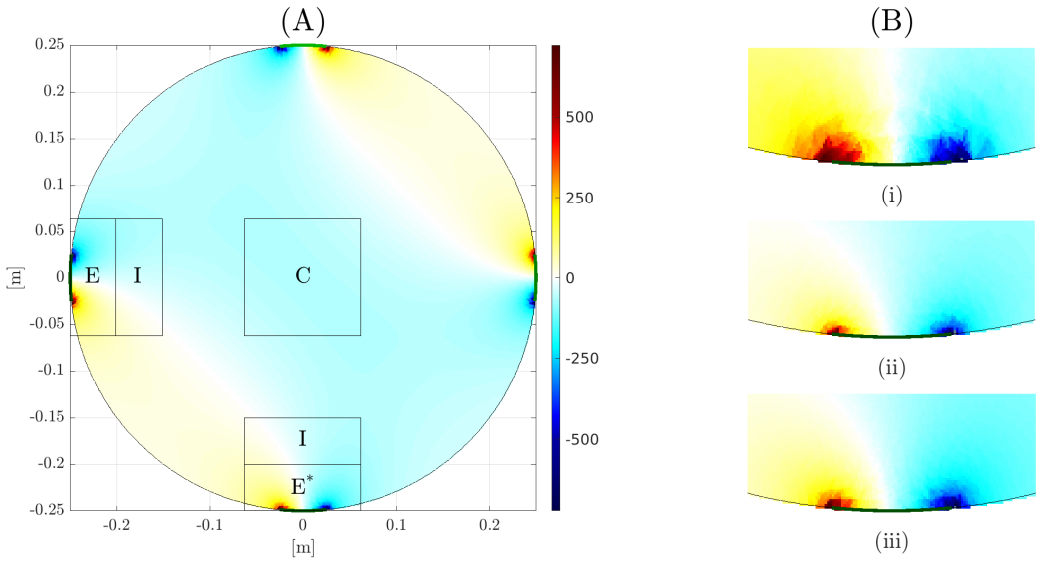

Figure 4.5: (A) Sensitivity distribution for the reference mesh (C15) generated in Gmsh with regions of interest used to compare between models. (B) 3 sensitivity distributions in region E^* next to the electrodes: (i) Constant mesh M1 (ii) refined mesh M15 with a balance point of 82% (iii) reference mesh from (A).

mesh parameters for odd numbered meshes can be seen in table 4.1. Across all meshes the measurement error when computing the voltage measurements was insignificant at less than 0.2%.

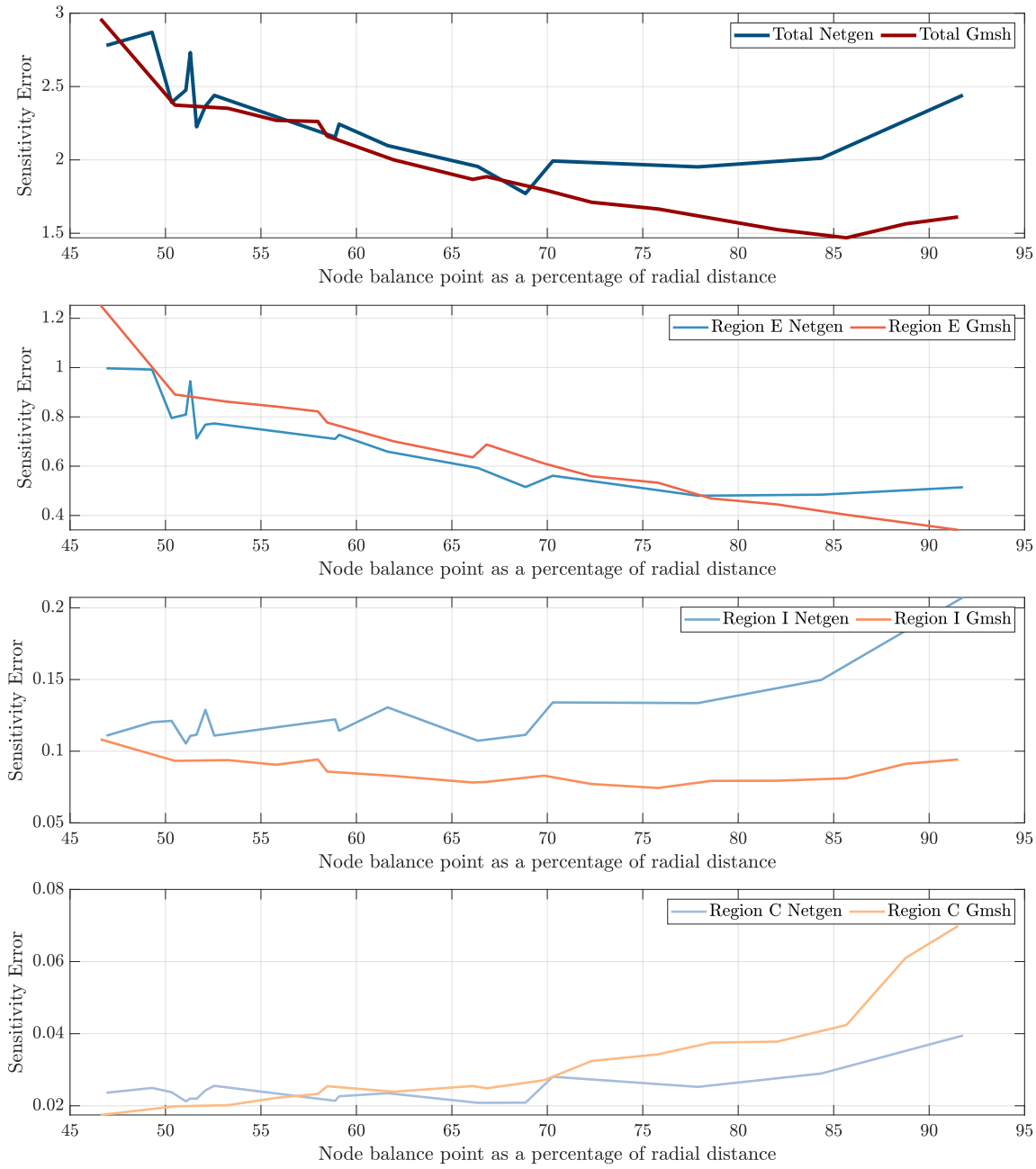

Figure 4.6: Resulting sensitivity error for Netgen (blue) and Gmsh (red) as the balance of the nodes was shifted towards the electrodes. From top to bottom: total sensitivity error, the sum of sensitivity error in region E, the sum of sensitivity error in region I and the sum of sensitivity error in region C. The regions are described in figure 4.5.

4.5 Discussion

We consider several questions on the requirement of FEM refinement in the neighbourhood of electrodes and the available tools for mesh refinement in EIT. 1) Given a "FEM element budget", what should balance of nodes be between the centre of the model and the electrodes? 2) How do different freely available meshing tools that are commonly used with EIT compare when used to refine 3D meshes?

While refining meshes surrounding the electrodes is agreed to be useful, there is a lack of systematic analysis of the required refinement level, and controlling such refinement is difficult. Automatic mesh refinement is an area of active work and there are a number of commercial and free products available. We compare two programs used widely in EIT. Our results show that Netgen and Gmsh control mesh refinement differently and the same input parameters result in meshes with different numbers of nodes. figure 4.2, depicts the difference in mesh dissipation rates between Netgen and Gmsh. The mesh size in Gmsh increased gradually from the surface of the electrode towards the centre of the model, where the mesh size in Netgen increased much more quickly from the edges of the electrode. While we attempted to control the dissipation rate in Netgen by manipulating the mesh density in the centre of the model, we were unable to achieve a smooth transition between the electrode and internal regions of the mesh.

To analyze the benefit of electrode refinement and the difference between Netgen and Gmsh refinement techniques we consider a sequence of refined meshes compared to a "gold standard", uniformly fine FEM solution. The models were refined either globally or in the electrode neighbourhood, and the error in the sensitivity matrix

J was compared. figure 4.4 displays the difference in sensitivity between constant meshes and meshes with refinement at the electrodes. The sensitivity error was lower in Netgen across all constant refinement meshes, in part because there were more total nodes than Gmsh meshes with the same number of nodes on the electrode. Refinement around the electrode decreased the total sensitivity error, but still had larger error than meshes with constant refinement due to the smaller number of nodes in the model.

Using the balance point analysis, we were able to determine the optimal distribution of nodes to minimize sensitivity in both Gmsh and Netgen. The minimum total sensitivity from figure 4.6 was approximately 70% for Netgen. This was mainly due to the rapid dissipation of node density away from the electrodes. Increasing the refinement near the electrode reduced error in region E, but in region I there were insufficient nodes to reduce the sensitivity error. As the balance of refinement approached 90% the error in region E also started to increase as the node density did not remain fine throughout the entire region. This effect can also be seen in figure 4.2. In Gmsh the optimal balance for refinement was at approximately 85% of the radial distance. Since mesh density was set to reduce evenly between the electrode surface and the centre of the model, there was a higher density of nodes that was maintained in regions E and I as the electrode refinement increased. The error in the centre of the model was higher in Gmsh meshes, but since this is where the sensitivity is lowest the total sensitivity error was much lower.

The ability to selectively control the mesh refinement in regions in Gmsh also allows users to generate complex meshes and control mesh density surrounding internal

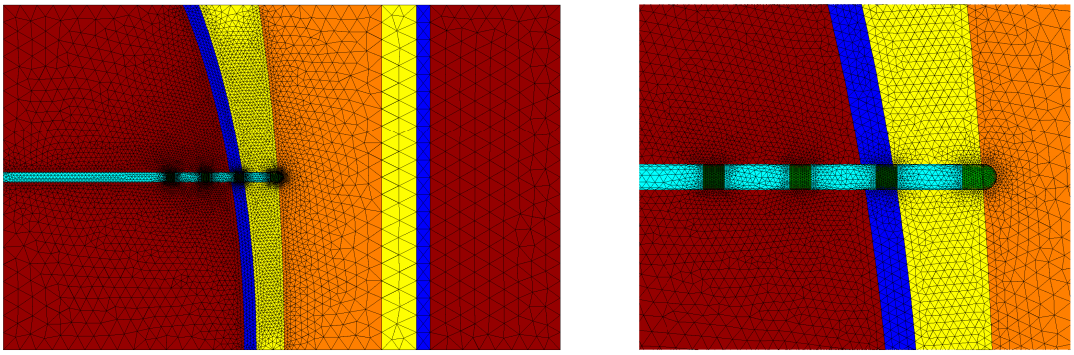

Figure 4.7: Example FEMs of a probe entering a bone from the surrounding tissue. Refinement is specified around the electrodes and tissue interfaces near the probe.

structures and electrodes an example mesh is shown in figure 4.7 where a model was created of a probe entering a bone from the surrounding tissue. These additions fill an important need in EIT to allow for more accurate models of regions surrounding internal structures and electrodes, and

Despite the increased ability to control refinement, the results still show that there are discrepancies between the specified parameters and the resulting meshes. The data in table 4.1 show that the maximum element lengths specified for each mesh were different from the actual maximum edge lengths. As the node density was increased near the electrodes, in Netgen the balance point did not always shift towards the electrode as the maximum node density was not always higher despite specifying a smaller mesh size. In Gmsh the mesh density was closer to the specified values, typically resulting in more nodes in the refined meshes.

Across both analyses errors away from the refined areas may be higher, but the ability to refine meshes selectively near regions where high sensitivity is required may allow for reduced measurement error while still allowing for quicker meshing

times. As more electrodes are added and the model complexity is increased, we expect that refinement around the electrodes will continue to reduce total sensitivity error. However the node balance analysis will not be possible for irregularly shaped models. The node balance analysis provides a straightforward method to determine the ideal placement of a given number of nodes to reduce model errors.

4.6 Summary

In this paper we examine the requirement for mesh refinement around electrodes in Electrical Impedance Tomography (EIT). While it has been recommended that models be refined around the electrodes, where current density and sensitivity are highest, the level of refinement required is poorly understood. Using a set number of nodes, we investigate the optimal distribution between the electrodes and the volume of a model. A balance point is used to measure the difference in distribution between the electrode and the centre of the model. To calculate this, all nodes contained between the surface of a selected electrode and the centre of the model were identified and the mean position of nodes along the container axis was computed. We compare refinement strategies across commonly used meshing software in EIT and compare the model sensitivity error to an ultra-fine reference mesh. In a tank model, for a fixed number of nodes, error in the sensitivity calculation is minimized when the balance point of the nodes is n 85% of the tank radius and the node density dissipates evenly from the electrode surface to the centre of the model. Using this method sensitivity error was decreased in all regions with high sensitivity. This node

distribution technique enables the generation of accurate meshes with fewer nodes that can reduce measurement error and computing time.